Adaptation of turnip mosaic virus to *Arabidopsis thaliana* involves rewiring of VPg - host proteome interactions

José L. Carrasco[1], Pablo A. Gutiérrez[2], Santiago F. Elena[1,3,*]

[1]Instituto de Biología Integrativa de Sistemas (CSIC - Universitat de València), Paterna, 46182 València, Spain.

[2]Laboratorio de Microbiología Industrial, Facultad de Ciencias, Universidad Nacional de Colombia, Medellín, Colombia.

[3]The Santa Fe Institute, Santa Fe NM87501, USA.

[*]Correspondence, e-mail: santiago.elena@csic.es.

ORCIDs:

J.L.C. https://orcid.org/0000-0002-5905-8042

P.A.G. https://orcid.org/0000-0002-7003-6485

S.F.E. https://orcid.org/0000-0001-8249-5593

Keywords: experimental evolution; protein-protein interactions; targets of adaptation; virus evolution

Abstract

The outcome of a viral infection depends on a complex interplay between the host physiology and the virus, mediated through numerous protein-protein interactions. In a previous study we used high-throughput yeast two-hybrid (HT-Y2H) to identify proteins in *Arabidopsis thaliana* that bind to the proteins encoded by the turnip mosaic virus (TuMV) genome. Furthermore, after experimental evolution of TuMV lineages in plants with mutations in defense-related or proviral genes, most mutations observed in the evolved viruses affected the VPg cistron. Among these mutations, D113G was a convergent mutation selected in many lineages across different plant genotypes. In contrast, mutation R118H specifically emerged in the *jin1* mutant with affected jasmonate signaling. Using the HT-Y2H system, we analyzed the impact of these two mutations on VPg's interaction with plant proteins. Interestingly, both mutations severely compromised the interaction of VPg with the translation initiation factor eIF(iso)4E, a crucial interactor for potyvirus infection. Moreover, mutation D113G, but not R118H, adversely affected the interaction with RHD1, a zinc-finger homeodomain transcription factor involved in regulating DNA demethylation. Our results suggest that RHD1 enhances plant tolerance to TuMV infection.

46 **1. Introduction**

47 Viruses establish multiple contact points with the host proteome, primarily through a
48 limited number of proteins, particularly reduced in the case of RNA viruses (Belshaw,
49 Pybus and Rambaut 2007; Mahmoudabadi et al. 2018). This interaction involves virus-
50 host protein-protein interactions (PPIs) that result in the manipulation of various cellular
51 pathways for creating favorable replication conditions. This manipulation can occur by
52 sequestering cell resources for the virus's benefit or by interfering with immune
53 responses. Simultaneously, host cell receptors play a role in sensing foreign elements
54 and responding accordingly. Recent years have seen significant progress in creating
55 detailed, high-quality maps of virus-host PPIs (Uetz et al. 2006; de Chassey et al. 2008).
56 Integrative approaches have identified both general and specific molecular mechanisms
57 employed by different viruses (Dyer et al. 2008; Mukhtar et al. 2011; Pichlmair et al.
58 2012; Ahmed et al. 2018; Aguirre and Guantes 2023). These findings, coupled with
59 additional omics data, have been used to predict phenotypic outcomes of infection
60 (Tisoncik-Go et al. 2016; Cervera et al. 2018; Tarazona, Forment and Elena 2020). These
61 advancements build upon the continuous development of a comprehensive large-scale
62 map of host PPIs, which, while not fully complete, proves valuable in recognizing
63 disease-associated modules (Mukhtar et al. 2011; Menche et al. 2015).

64 In a previous study Martínez et al. (2023) systematically identified direct PPIs
65 between turnip mosaic virus strain YC5 (TuMV; species *Turnip mosaic virus*, genus
66 *Potyvirus*, family *Potyviridae*) and one of its natural hosts, *Arabidopsis thaliana* (L.)
67 HEYNH, using high-throughput yeast two-hybrid (HT-Y2H) screenings. This study
68 uncovered 378 new PPIs between TuMV and plant proteomes. Among the viral proteins,
69 the RNA-dependent RNA polymerase NIb emerged with the highest number of contacts,
70 including crucial salicylic acid (SA)-dependent transcription regulators. The authors
71 constructed and analyzed a network consisting of 399 TuMV-*A. thaliana* interactions,
72 incorporating intravirus and intrahost connections. Notably, their findings revealed that
73 TuMV-targeted host proteins (*i*) were enriched in various aspects of plant responses to
74 infections, (*ii*) exhibit greater connectivity, (*iii*) had enhanced capacity to disseminate
75 information throughout the cell proteome, (*iv*) showed higher expression levels, and (*v*)
76 were under stronger purifying selection than expected by chance.

77 In previous evolution experiments with potyviruses, the VPg cistron has been
78 identified as a significant target of selection. For instance, Agudelo-Romero *et al*. (2008)
79 observed that a single amino acid replacement in VPg significantly increased tobacco

80 etch virus (TEV) infectivity, severity of symptoms, and viral load in *A. thaliana*. Later
81 on, Hillung et al. (2014) further described additional VPg mutants in several *A. thaliana*
82 ecotypes that differed in their susceptibility to TEV infection. Likewise, Navarro et al.
83 (2022) and Ambrós et al. (2024) evolved TuMV lineages in different defense-deficient
84 genotypes of *A. thaliana*, observing pervasive mutations affecting VPg, with remarkable
85 examples of parallel evolution with the same mutations fixing in lineages evolved in the
86 same host genotype. Gallois et al. (2010) found that *A. thaliana* plants with knock-out
87 mutations in the *EUKARYOTIC TRANSLATION INITIATION FACTORS (ISO)4E*,
88 *(ISO)4G1* and *(ISO)4G2* (*eIF(iso)4E*, *eIF(iso)4G1* and *eIF(iso)4G2*, respectively) genes
89 were resistant to TuMV infection, demonstrating the proviral role of these eIFs.
90 However, two mutations in VPg were sufficient to overcome this resistance and revert to
91 the original infection phenotype. Notably, Y2H assays showed that these mutations did
92 not preclude the binding of VPg to eIF(iso)4E (Gallois et al. 2010). As another example,
93 the *pvr2* locus, one of the most extensively used resistance genes against potato virus Y
94 (PVY) in pepper cultivars, encodes the eIF4E factor, which physically interacts with VPg.
95 Interestingly, all resistance-breaking viral isolates identified so far contain mutations in
96 the VPg cistron (Duprat et al. 2002; Moury et al. 2004; Ayme et al. 2006).
97 VPg has been described as a scaffolding protein that interacts with other potyviral
98 proteins (Bosque et al. 2014; Hafrén, Löhmus and Mäkinen 2015) and with many host
99 proteins (Martínez et al. 2016, 2023), most notably factors involved in genome
100 transcription, being linked to the 5'-end of the viral genome and providing the hydroxyl
101 group that primes the synthesis of complementary strands by the viral NIb replicase
102 (Eskelin et al. 2011). Additionally, it plays a role in protein synthesis by directly
103 interacting with canonical translation factors eIF(iso)4E and eIF(iso)4G (Gallois et al.
104 2010; Hafrén, Löhmus and Mäkinen 2015) and with the antiviral factor eIF4E1 that
105 protects the translational machinery during TuMV infection (Zafirov et al. 2023). Indeed,
106 Martínez et al. (2023) HT-Y2H analyses and literature curation resulted in the
107 identification of 43 direct interactors, involved in diverse cellular processes. Amongst
108 the most highly expressed and connected genes, *CALNEXIN 1* (*CNX1*) and *OBERON 1*
109 (*OBE1*) were shown to directly interact with VPg. Both CNX1 and OBE1 proteins were
110 proviral factors whose knocked-out expression resulted in late and less severe symptoms.
111 Other genes such as *NONEXPRESSER OF PATHOGENESIS-RELATED GENES 1*
112 (*NPR1*), *SUMO 3* (*SUM3*), *SUMO CONJUGATING ENZYME 1* (*SCE1*), and specially

113 *TGACG SEQUENCE-SPECIFIC BINDING FACTOR 1* (*TGA1*) also resulted in milder
114 disease symptoms, although their interaction with VPg was mediated by NIb.
115 In various evolution experiments of TuMV isolate YC5 in different *A. thaliana*
116 genotypes, it has consistently been observed that VPg fixed nonsynonymous mutations;
117 14 identified as being subject to positive selection (González, Butković, and Elena 2019;
118 González et al. 2021; Navarro et al. 2022; Melero, González, and Elena 2023; Ambrós et
119 al. 2024). The majority of these positively selected mutations are concentrated within a
120 helix-coil-helix structural domain, spanning amino acids 110 to 120 [Fig. 4B in Ambrós
121 et al. (2024)]. Certain mutations were consistently present across lineages that evolved
122 in different host genotypes and environmental conditions. For instance, the VPg^{D113G}
123 mutation was observed in lineages evolved in nine distinct plant genotypes, including
124 wild-type Col-0 plants, and two environmental conditions (González, Butković, and
125 Elena 2019; González et al. 2021; Navarro et al. 2022; Ambrós et al. 2024). Conversely,
126 some mutations were specific to particular host genotypes, such as the VPg^{R118H} mutation,
127 found exclusively in lineages evolved in mutants of *JASMONATE INSENSITIVE 1* (*JIN1*)
128 and *DECREASED DNA METHYLATION 1* (*DDM1*) genes, both being particularly
129 permissive to TuMV infection (Navarro et al. 2022; Ambrós et al. 2024).
130 Given the prominent role played by VPg during potyvirus infections, its apparent
131 prominence as target of natural selection and its promiscuous interaction with other
132 potyviral and host proteins, a question that immediately arises from all previously
133 mentioned studies is the extent to which these mutations affect the ability of VPg to
134 engage into PPIs resulting in fitness increases. To tackle this question, we have selected
135 mutants VPg^{D113G} and VPg^{R118H} as examples of what can be considered generalist and
136 specialist versions of VPg, respectively. The two VPg mutants were cloned and used as
137 bait proteins in HT-Y2H experiments to identify host interactors that differ from those
138 obtained for VPg^{wt} by Martínez et al. (2023). Then, the relative affinity of the differential
139 interactors was evaluated by a quantitative assay and compared with the VPg^{wt}. To
140 further characterize the effect of these mutations in TuMV performance, we inoculated
141 *eif(iso)4e* and *ros1-associated homeodomain protein 1* (*rhd1*) mutant plants and
142 characterized disease progression and viral accumulation. Finally, we performed *in silico*
143 evaluations of the effect of the two mutations of interest in VPg folding and used docking
144 and molecular dynamics techniques to evaluate their effect on the interaction with
145 eIF(iso)4E and RHD1.
146

147

148 ## 2. Materials and Methods

149 ### 2.1. Plasmid construction

150 The mutated variants of the VPg cistron were amplified by PCR using Phusion High-
151 Fidelity DNA polymerase (Thermo Scientific, Waltham MA, USA) according to
152 manufacturer's recommendations and using primers specifically designed for the In-
153 Fusion cloning system (Takara Bio, Mountain View CA, USA). The amplified PCR
154 fragments were recombined into the yeast bait two-hybrid vector pGBKT7 (Takara Bio,
155 Kusatsu, Japan), previously digested with *Eco*RI and *Bam*HI, using the In-Fusion
156 enzyme. Thus, translational fusions of all three VPg protein variants (bait protein) with
157 the GAL4 DNA-binding domain were generated.

158

159 ### 2.2. High-throughput yeast two-hybrid screening

160 To search for differential interactors among the original VPg protein and the two selected
161 mutated variants, an *A. thaliana* Col-0 cDNA library (Takara Bio) transformed into the
162 *Saccharomyces cerevisiae* Y187 strain (prey strain) was screened using the Matchmaker®
163 Gold Yeast Two-Hybrid System (Takara Bio). For that purpose, the three bait VPg
164 proteins cloned in pGBKT7 were transformed in the yeast strain Y2HGold. Then, the
165 Y187 prey strain was mated to each of the Y2HGold haploid bait strains expressing the
166 wild-type and the mutated variants of VPg protein and plated on a double dropout medium
167 (SD/-Leu/-Trp) containing 40 μg/mL X-α-Gal and 200 ng/mL aureobasidin A. Co-
168 transformants displaying α-galactosidase activity were subjected to a second round of
169 selection on a quadruple dropout medium (SD/-Leu/-Trp/-Ade/-His) also containing X-
170 α-Gal. Plasmids pGBKT7-T-antigen, pGADT7-laminin C, and pGADT7-murine p53
171 (Takara Bio) were used as negative controls. cDNA inserts from positive yeast clones
172 were amplified by colony PCR, digested with *Alu*I and analyzed by agarose gel
173 electrophoresis to eliminate duplicate clones. Selected prey plasmids were rescued using
174 a glass-bead extraction protocol and transformed into *Escherichia coli* DH5α for
175 amplification and sequencing. DNA and protein sequence analyses were performed with
176 the WU-BLAST algorithm. For each positive interaction, the prey plasmid was re-
177 transformed into the yeast strain Y2HGold and mated to all three bait strains and also to
178 a control Y187 yeast strain transformed with the empty pGBKT7 vector to remove false
179 positives.

180

181 **2.3. Plant genotypes, virus clones and inoculation procedures**

182 Wild-type and two *A. thaliana* mutants were used in this study, all in the same Col-0
183 background. Seeds of the T-DNA insertion line SALK_092897C (*rhd1-1* mutant) were
184 obtained from the Nottingham Arabidopsis Stock Center (NASC), whereas *eif(iso)4e*
185 seeds were a kind gift from Dr. Jean-Luc Gallois (INRA, Avignon, France) (Duprat et al.
186 2002).

187 TuMV infectious sap was obtained from TuMV-infected *Nicotiana benthamiana*
188 DOMIN plants inoculated with the infectious plasmid p35STunos that contains a cDNA of
189 the TuMV genome isolate YC5 from calla lily (*Zantesdeschia* sp) (GeneBank
190 AF530055.2) under the control of the cauliflower mosaic virus 35S promoter and the *nos*
191 terminator (Chen et al. 2003) as described elsewhere (González, Butković and Elena
192 2019; Corrêa et al. 2020). After plants showed symptoms of infection, they were pooled
193 and frozen with liquid N_2. This frozen plant tissue was homogenized into a fine powder
194 using a Mixer Mill MM400 (Retsch GmbH, Haan, Germany). For inoculations, 0.1 g of
195 powder was diluted in 1 mL inoculation buffer [50 mM phosphate buffer (pH 7.0), 3%
196 PEG6000, 10% Carborundum] and 5 µL of the inoculum was gently rubbed onto two
197 leaves per plant. As a control, another set of plants were mock-inoculated only with
198 inoculation buffer. Plants were all inoculated when they reached growth stage 3.5 in the
199 Boyes et al. (2001) scale. This synchronization ensures that all hosts were at the same
200 phenological stage when inoculated.

201 VPg mutations D113G and R118H were introduced by site-directed mutagenesis in
202 the p35STunos plasmid using the Quikchange II XL kit (Agilent Technologies, Santa
203 Clara CA, USA) and following the indications of the manufacturer, resulting in plasmids
204 p35STunos-VPg^{D113G} and p35STunos-VPg^{R118H}. Plasmids were purified using the
205 ZymoPURE II Plasmid Miniprep kit (Zymo Research, Irving CA, USA) and resuspended
206 in sterile water.

207 For evaluation of the mutated VPg alleles, wild-type, *eif(iso)4e* and *rhd1-1* plants
208 were inoculated with p35STunos, p35STunos-VPg^{D113G} and p35STunos-VPg^{R118H}. One
209 leaf per plant was inoculated by gentle abrasion after applying 3 µg of plasmid DNA
210 diluted in 6 µL of water supplemented with 10% Carborundum.

211

212 **2.4. Infectivity, symptoms progression and quantification of viral load**

213 The number of infected symptomatic plants, out of 20, as well as the severity of symptoms
214 in a semi-quantitative scale in which zero means no symptoms and 5 systemic necrosis
215 [Fig. 1 in Butković et al. (2021)] were monitored every day until 14 days post-inoculation
216 (dpi). As a control, another set of mock-inoculated plants was treated in the same way.
217 Viral loads were measured 12 dpi in four different pools of five infected plants each,
218 by absolute real-time quantitative RT-PCR (RT-qPCR) using a TuMV standard curve and
219 the primers TuMV F117-fw ($^{5'}$CAATACGTGCGAGAGAAGCACAC$_{3'}$) and F118-rv
220 ($^{5'}$TAACCCCTTAACGCCAAGTAAG$_{3'}$) that amplify a 173 nucleotides fragment from
221 the CP cistron of TuMV genome, as previously described (Corrêa et al. 2020). Briefly,
222 standard curve consisted of nine serial dilutions of the *in vitro* synthesized TuMV genome
223 prepared in total plant RNA purified from healthy *A. thaliana* plants. Amplification
224 reactions were run in a 20 µL volume using the qPCRBIO SyGreen 1-step Go Hi-ROX
225 System (PCRBiosystems, London, UK) and the recommended manufacturer's
226 instructions in an ABI StepOne Plus Real-time PCR System (Applied Biosystems, Foster
227 City CA, USA). An initial RT phase of 10 min at 45 ºC and 2 min at 95 ºC was followed
228 by a PCR stage with the following cycling conditions: 40 cycles of 5 s at 95 ºC and 25 s
229 at 60 ºC, and a final melting curve profile analysis that consisted of 15 s at 95 ºC, 1 min
230 at 60 ºC and 15 s at 95 ºC. As negative controls, total plant RNA (noninfected control)
231 and water were included in the analysis. Quantitative reactions were run as three
232 technical replicates per sample and results were analyzed using the StepOne software
233 2.2.2 (Applied Biosystems).
234
235 **2.5. Determination of TuMV consensus sequence**
236 The consensus sequences of the viral genomes accumulated at the end of the infection
237 processes were generated as described elsewhere (*e.g.*, Navarro et al. 2022). In short,
238 total RNAs were obtained and amplified by high-fidelity RT-PCR using the AccuScript
239 Hi-Fi (Agilent Technologies) reverse transcriptase and Phusion DNA polymerase
240 (Thermo Scientific) following the manufacturer's instructions. Each complete TuMV
241 genome was amplified as three overlapping amplicons using three specific sets of primers
242 and the amplification conditions described in Navarro et al. (2022). PCR products were
243 purified with the MSB Spin PCRapace kit (Stratec Molecular, Coronado CA, USA) and
244 then Sanger-sequenced by Novogene Europe Co. Ltd. (Cambridge, UK). Full-length
245 consensus viral sequences were obtained assembling the sequences of the three amplified

246 products by using the Genious R9.0.2 program (Dotmatics, Bishop's Stortford, UK). No
247 additional mutations were found in any of the VPg clones.
248
249 **2.6. Host gene expression analysis by relative RT-qPCR**
250 For the analysis of *RHD1* and *TGA1* expression, RNA was purified with the Quick-RNA
251 Plant Miniprep kit (Zymo Research) following the protocol recommended by the
252 manufacturer. RT-qPCR was performed in an ABI OneStep Plus Real-time PCR System
253 (Applied Biosystems) from 50 ng RNA using the qPCRBIO SyGreen 1-step Go Hi-ROX
254 System from (PCRBiosystems). The *AT1G13320* corresponding to the *PROTEIN*
255 *PHOSPHATASE 2A SUBUNIT A3* (*PP2AA3*) gene was used as endogenous reference
256 (Czechowski et al. 2005). The primers used for the amplification were pp2aa3-fw
257 ($^{5'}$TTGGTGCTCAGATGAGGGAGAG$_{3'}$), pp2aa3-rv
258 ($^{5'}$TTCACCAGCTGAAAGTCGCTTAG$_{3'}$), rhd1-fw
259 ($^{5'}$TATCGGAACCACCGCTTACG$_{3'}$), rhd1-rv ($^{5'}$CGGTGGAAGTTACGGTGACA$_{3'}$),
260 tga1-fw ($^{5'}$ACGAACCTGTCCATCAATTCGG$_{3'}$), and tga1-rv
261 ($^{5'}$CCATGGGAAGTATCCTCTGACACG$_{3'}$). For expression in leaves, plants were
262 grown for about 4 weeks [growth stage ~3.70 in the Boyes et al. (2001) scale].
263
264 **2.7. Statistical analyses**
265 Quantitative specificity α-galactosidase assays were conducted per interactor and VPg
266 allele, with repetitions ranging from 1 to 5 times (median 2) in independent blocks. To
267 mitigate potential block effects, individual measures were normalized by the mean of the
268 VPg^{wt} allele estimated in the corresponding block. Normalized data underwent analysis
269 using Welch's robust one-way ANOVA, and effect magnitudes were assessed using the
270 η^2 statistic. Conventionally, $\eta^2 < 0.05$ are considered small, $0.05 \leq \eta^2 < 0.15$ as medium,
271 and $\eta^2 \geq 0.15$ as large effects.
272 Relative expression data for *RHD1* and *TGA1* were fitted to a generalized linear
273 model (GLM) with infection status (mock-inoculated *vs*. TuMV-VPg^{wt} infected) and days
274 post-infection (dpi) as orthogonal factors, utilizing a Gamma distribution and log-link
275 function. In this context, the magnitude of effects was assessed using the η_P^2, with similar
276 criteria than for η^2 above.
277 The number of infected plants, out of 20, observed for wild-type and *rhd1* plants
278 were independently analyzed using Kaplan-Meier regression. Pairwise comparisons of
279 the median time to the appearance of first symptoms for each VPg allele were performed

280 using log-rank tests. Symptom severity progression data were independently fitted to
281 repeated-measures ANOVAs, with dpi as an intra-individual factor and VPg allele as an
282 inter-individual factor. The magnitude of effects was evaluated using the η_P^2 statistic.
283 Viral load data were fitted to a GLM with plant genotype and VPg allele as
284 orthogonal factors, and experimental block nested within the interaction of the two
285 orthogonal factors, employing a Gaussian distribution and identity-link function. The
286 magnitude of effects was assessed using the η_P^2 statistic.
287 In all reported pairwise *post hoc* tests, the Bonferroni sequential method was
288 applied.
289
290 **2.8. Homology modelling**
291 Models were generated with MODELLER version 10.4 (Webb and Sali, 2016). For the
292 *A. thaliana* eIF(iso)4E, and its paralogs eIF4E and nCBP, the X-ray structures of eIF4E
293 from *Cucumis melo* (Miras et al. 2017), *Pisum sativum* (Ashby et al. 2011), and *Mus*
294 *musculus* (Rydzik et al. 2017; Wan et al. 2020; Wojcik et al. 2021) were used as templates
295 (Supplementary Fig. S1). The model of the VPg protein from TuMV was inferred using
296 the NMR structure of the PVY homolog (Coutinho de Oliveira et al. 2019). Input
297 alignments were generated with MUSCLE (Edgar, 2004). In each case, the model lowest-
298 energy model out of 100 structures was selected and submitted to a final round of
299 refinement using ROSETTA's relax protocol (Conway et al. 2013).
300
301 **2.9. Docking**
302 Docking was performed with the Monte Carlo based multi-scale docking algorithm
303 implemented in RosettaDock (Chaudhury et al. 2011). In each case, high-energy
304 rotamers were removed prior to docking using the Docking Prepack application from
305 ROSETTA (Wang et al. 2005). For the eIF(iso)4E and VPg docking model, structures
306 were prepositioned near each other with the binding pockets facing each other using
307 HADDOCK (Dominguez et al. 2003; van Zundert et al. 2016; Honorato et al. 2021). In
308 this case, ambiguous interaction restraints (AIRs) were generated using a combination of
309 NMR chemical shift perturbations (Coutinho de Oliveira et al. 2019), mutagenesis data
310 on the eIF4E/eIF(iso)4E - VPg system (Monzingo et al. 2007; Roudet-Tavert et al. 2007;
311 German-Retana et al. 2008; Ashby et al. 2011; Pérez et al. 2012; Svanella-Dumas et al.
312 2014), and experimental data from Martínez et al. (2023). Unfolded and mobile regions

313 were removed from both proteins and docking site constraints for residues known to be
314 in contact in the eIF(iso)4E/VPg interaction were included in local docking protocol
315 (Supplementary Fig. S2). A total of 1000 decoys were generated during the docking
316 perturbation runs. Residues in the interface of the selected model were refined using a
317 high-resolution full atom minimization protocol (Conway et al. 2013). After this step,
318 the mobile regions of VPg and eIF(iso)4E were included using MODELLER, and an
319 optimal conformation was recalculated using the kinematic closure method in ROSETTA
320 (Mandell et al. 2009) (Supplementary Fig S2). The final complex was further refined
321 using a molecular dynamic simulation in explicit solvent with NAMD (Phillips et al.
322 2020). This step was performed using periodic boundary conditions in a water box with
323 a 10 Å padding, 0.15 M NaCl, and a temperature of 298 K (Spivak et al. 2023). Docking
324 of RHD1 and the VPg protein was performed using a global docking protocol using the
325 AlphaFold RHD1 model available at Uniprot (Jumper et al. 2021). Docking was
326 performed separately on N- and C- terminal Zn-finger and homeobox domains,
327 respectively. After minimization, structures were fitted using a global docking protocol
328 using 10,000 decoys for each RHD1 domain. Other RHD1 PPIs were pulled out from
329 STRING database version 12.0 (Szklarczyk et al. 2023).
330
331

332 3. Results and Discussion

333 3.1. HT-Y2H screens and evaluation of differences in affinity between VPg variants 334 and host interactors

335 Three screens were conducted in parallel using wild-type and two mutated VPg variants,
336 D113G and R118H, as the respective bait proteins. The number of clones screened
337 ranged from $2 \cdot 10^7$ to $2.5 \cdot 10^7$ per variant, with a mating efficiency of 30% to 35%.
338 Initially, approximately 400 clones were selected, from which six for VPg^{wt}, seven for
339 VPg^{D113G}, and eight for VPg^{R118H} were further validated through a second round of more
340 rigorous selection and semiquantitative evaluation of binding specificity after plasmid
341 rescue and yeast retransformation. Subsequently, a quantitative α-galactosidase activity
342 assay was performed with the selected clones. Only clones displaying significant
343 statistical differences among alleles were subjected to gene identification through
344 sequencing. Following sequencing, two clones selected for VPg^{D113G} corresponded to
345 *AT5G42780*, while two clones selected for VPg^{wt} matched with *AT5G35620*.

346 Consequently, we identified 19 host proteins that interact differentially among the three
347 VPg alleles.

348 Fig. 1 depicts a heatmap constructed based on the binding affinities similarity
349 matrix among the 19 host proteins and the three VPg alleles. Among the interactors, nine
350 exhibited a significant overall difference among the three VPg alleles (Supplementary
351 Fig. S3). The smallest significant effect was observed with *AT2G19270*, which encodes
352 the *PROLINE RICH MITOTIC CHECKPOINT CONTROL FACTOR* (*PRCC*). PRCC is
353 involved in regulating protein modifications and signal transductions (Welch's robust
354 ANOVA: $F_{2,25.451} = 4.326$, $P = 0.024$, $\eta^2 = 0.171$). On the other hand, the most substantial
355 effect was observed with *AT5G35620*, the locus encoding the well-characterized VPg
356 interactor eIF(iso)4E protein ($F_{2,67.604} = 675.852$, $P < 0.001$, $\eta^2 = 0.958$).

357 Applying Bonferroni *post hoc* pairwise difference tests, we compared the affinity
358 values between VPg^{wt} and each of the 19 host interactors with those observed for the two
359 VPg mutant alleles, revealing a remarkably diverse pattern of effects. As illustrated in
360 Fig. 1, these 19 proteins can be categorized into three distinct groups. In the following
361 discussion, we will delve into the host proteins exhibiting differential binding strength
362 with the VPg alleles. The first group comprises two proteins whose interactions are
363 significantly more robust with VPg^{wt} than with either of the two mutant alleles. These
364 proteins are: (*i*) the aforementioned eIF(iso)4E ($P < 0.001$; 90.50% weaker interaction)
365 and (*ii*) the FRUCTOKINASE-LIKE 1 (FLN1) protein, a member of the pfkB-
366 carbohydrate kinase family encoded by locus *AT3G54090* ($P < 0.001$; 36.54% weaker
367 interaction). FLN1 serves as a potential plastidial target of thioredoxin z and is crucial
368 for proper chloroplast development. Its role extends to the regulation of plastid-encoded
369 polymerase (PEP)-dependent chloroplast transcription. Consequently, *fln1* mutants
370 exhibit aberrant chloroplast development, general developmental defects, and impaired
371 PEP-dependent transcription (Gilkerson et al. 2012).

372 The second group in Fig. 1 is the most heterogeneous, encompassing three host
373 proteins that exhibit either no differences with VPg^{wt} or variable effects with VPg^{D113G}
374 and VPg^{R118H}. (*i*) The *AT5G62580* locus encodes ARM-REPEAT SUPERFAMILY
375 PROTEIN and demonstrates a 28.76% reduction in binding strength with VPg^{D113G}
376 compared to VPg^{wt} ($P = 0.025$), while it shows no significant effect on VPg^{R118H} ($P =$
377 1.000). This family of proteins binds to microtubules, impacting cellular organization
378 and organ growth (Buschmann et al. 2004). Intriguingly, Martínez et al. (2023) described
379 this protein as an interactor of NIb replicase. (*ii*) The second protein in this group is

380 RHD1 (encoded by *AT5G42780*). RHD1, a zinc finger and homedomain (ZF-HD)
381 protein, interacts with ROS1-ASSOCIATED METHYL-DNA BINDING PROTEIN 1
382 (RMB1), ROS1-ASSOCIATED WD40 DOMAIN-CONTAINING PROTEIN (RWD40)
383 and REPRESSOR OF SILENCING 1 (ROS1) in a multiprotein complex involved in the
384 base excision repair pathway through DNA methylation. This interactor was not
385 described by Martínez et al. (2023). Interestingly, RHD1 interacts with the transcriptional
386 regulator TGA1, known to act as a proviral factor via its interaction with NIb (Martinez
387 et al. 2023). RHD1 exhibits a 22.62% decrease in binding affinity with VPg^{D113G} ($P <$
388 0.001) but a 17.35% increase with VPg^{R118H} ($P = 0.003$) compared to VPg^{wt}. (*iii*) The
389 third member of this group is the product of the *PRCC* gene, involved in the regulation
390 of protein modifications and signal transductions. While VPg^{D113G} shows no differences
391 in binding compared to VPg^{wt} ($P = 1.000$), VPg^{R118H} exhibits 22.5% stronger binding (P
392 $= 0.029$).
393 The third group in Fig. 1 comprises four host proteins that exhibit no differences in
394 affinity between VPg^{wt} and VPg^{D113G} but consistently show increased binding strength
395 with VPg^{R118H}. (*i*) The product of the gene *PYRUVATE ORTHOPHOSPHATE*
396 *DIKINASE (PPDK) REGULATORY PROTEIN 1* (*RP1*) (*AT4G21210*) demonstrates
397 47.15% stronger binding with VPg^{R118H}. RP1, a bifunctional serine/threonine kinase and
398 phosphorylase, is involved in the dark/light-mediated regulation of PPDK by catalyzing
399 its phosphorylation/dephosphorylation (Chastain et al. 2007). Notably, RP1 was not
400 described by Martínez et al. (2023). (*ii*) The second host protein in this group is
401 OBERON 1 (OBE1), encoded by locus *AT3G07780*; this interaction was previously
402 described by Martínez et al. (2023). OBE1, a nuclear PHD finger protein, interacts with
403 WRKY transcription factors, forming complexes that bind to histones (via the PHD
404 finger) and repress the transcription of many stress-responsive genes (Du et al. 2023).
405 (*iii*) The MITOCHONDRIAL GLYCOPROTEIN FAMILY PROTEIN encoded by locus
406 *AT1G15870* binds 36.19% more strongly with VPg^{R118H} than with VPg^{wt}. Unfortunately,
407 no information about the function of this glycoprotein in the context of infection is
408 currently available. (*iv*) The MYOSIN 3 (MYOS3) protein encoded by locus
409 *AT3G58160*, a class XI myosin gene, is involved in the trafficking of Golgi stacks,
410 peroxisomes, and mitochondria in root hairs and leaf epidermal cells (Peremyslov et al.
411 2008). Class XI myosin genes have been shown to play important and diverse roles in
412 virus replication. For example, Amari et al. (2014) demonstrated that the inactivation of
413 myosin XI genes in *Nicotiana benthamiana* affected the functioning of the endoplasmic

414 reticulum, resulting in the aggregation of the movement protein of tobacco mosaic virus
415 and the altered intracellular distribution of the viral replicase. MYOS3 binds to VPg^{R118H}
416 27.51% more strongly than to the VPg^{wt} allele ($P = 0.007$).
417
418 **3.2. TuMV infection affects the expression of *RHD1* and *TGA1***
419 As outlined in the Introduction, VPg interacts with both the viral replicase NIb and the
420 host factor RHD1. Additionally, both NIb and RHD1 interact with the transcriptional
421 regulator TGA1, identified as a proviral factor by Martínez et al. (2023) for the first time.
422 To assess the impact of TuMV infection on the expression of these crucial genes, a time-
423 course analysis of *RHD1* and *TGA1* expression was conducted via relative RT-qPCR in
424 three pools of mock- and TuMV-VPg^{wt}-inoculated wild-type plants. Fig. 2 presents the
425 results of these experiments.
426 In the case of *RHD1*, overall effects were observed between infected and non-
427 infected plants (GLM: $\chi^2 = 28.568$, 1 d.f., $P < 0.001$, $\eta_P^2 = 0.814$) and across the
428 experimental time ($\chi^2 = 87.164$, 3 d.f., $P < 0.001$, $\eta_P^2 = 0.942$). More notably, a highly
429 significant interaction between these two factors was detected ($\chi^2 = 102.188$, 3 d.f., $P <$
430 0.001, $\eta_P^2 = 0.953$). This interaction is explained by gene expression in mock-inoculated
431 plants being consistently low and stable over time. In sharp contrast, expression in
432 infected plants was significantly lower (1.5- to 2.4-fold range; $P < 0.001$) at all time points
433 except at 6 dpi when *RHD1* expression surged 20-fold higher in infected plants ($P <$
434 0.001). Such pulse-like gene expression, is well suited for coordinating innate immune
435 antiviral responses, fine-tuning cellular processes without committing to prolonged
436 changes in gene activity (*e.g.*, Czerkies et al. 2018).
437 Concerning the effect of infection on *TGA1* expression, both infection status ($\chi^2 =$
438 100.553, 1 d.f., $P < 0.001$, $\eta_P^2 = 0.980$) and dpi ($\chi^2 = 39.247$, 3 d.f., $P < 0.001$, $\eta_P^2 = 0.953$)
439 had significant effects on *TGA1* expression levels. These effects are not independent (χ^2
440 $= 89.968$, 3 d.f., $P < 0.001$, $\eta_P^2 = 0.975$), as infected plants exhibit enhanced expression
441 over the time course. Maximum differences with non-infected plants were observed at
442 the two earlier time points (7.2- and 11.2-fold higher, respectively; $P < 0.001$), followed
443 by a reduction to non-significant differences at 9 dpi ($P = 0.570$) or a 1.9-fold higher
444 expression at the latest sampled time point ($P < 0.001$). This biphasic step-down
445 expression profile reflects a dynamic regulation of *TGA1* gene activity. The initial high
446 expression phase would be associated with an acute response to the initial infection, while

447 the reduction may represent a shift to a more sustained level of expression compatible
448 with TuMV overcoming defenses and stablishing a successful infection.
449 TGA1 regulates plant defense in a manner independent of NPR1 (Shearer et al.
450 2012). It accomplishes this by inducing the expression of key transcription factors, such
451 as *SYSTEMIC ACQUIRED RESISTANCE DEFICIENT 1* and *CALMODULIN-BINDING*
452 *PROTEIN 60g*. These transcription factors, in turn, target various essential regulators of
453 plant defense, including enzymes crucial for the synthesis of SA (Sun et al. 2018). Upon
454 a pathogen attack, SA levels surge, triggering two distinct responses: (*i*) the activation of
455 *NPR1*, leading to the expression of pathogenesis-related genes critical for reinforcing
456 systemic acquired resistance (SAR) against subsequent pathogen assaults (Zavaliev and
457 Dong 2023) and (*ii*) the enhancement of RNA-silencing antiviral defense (Alamillo,
458 Saénz and García 2006). Notably, despite the unaffected SAR in *tga1* plants, they exhibit
459 increased susceptibility to *Pseudomonas syringae* (Shearer et al. 2012). However, these
460 plants paradoxically display heightened resistance to TuMV infection (Martínez et al.
461 2023). This discrepancy raises intriguing questions about whether the activation of *TGA1*
462 during infection is a specific plant response or a consequence of a virus-induced
463 overexpression.
464
465 **3.3. *eif(iso)4e* resistance to TuMV infection is not affected by the three VPg alleles**
466 Sets of twenty plants of genotypes *eif(iso)4e* and wild-type were individually inoculated
467 with the three different VPg alleles. Daily records were kept for both the number of
468 infected plants and the severity of symptoms. A notable initial observation was that none
469 of the 20 *eif(iso)4e* plants exhibited any infection symptoms, irrespective of the VPg allele
470 carried by the inoculated TuMV. The possibility of this negative result being attributed
471 to failed inoculation trials was considered. To eliminate this potential explanation, an
472 additional 68 wild-type plants were inoculated with TuMV-VPg^{wt}. With a sample size of
473 88 wild-type plants, the probability of infecting a fully susceptible wild-type plant with
474 TuMV-VPg^{wt} was estimated based on the number of positive events (86) observed after
475 inoculating all the wild-type plants. Using the LaPlace point estimator and the adjusted
476 Wald 95% confidence interval method, the success rate was calculated to be 0.967 (0.916,
477 0.999). Therefore, even in the less favorable situation (*i.e.*, the lower limit of the
478 confidence interval), the likelihood of failing 20 independent inoculation events of fully
479 susceptible plants with a wild-type virus would be given by the Bernoulli process (1 –
480 $0.916)^{20} = 3.06 \cdot 10^{-22}$.

481 The same rationale was applied to the two mutant VPg alleles, where 20 out of 20
482 inoculated wild-type plants resulted in symptomatic infections. In this case, the LaPlace
483 estimation of success rate was 0.955 (0.859, 1.000), and the Bernoulli measure for the
484 less favorable situation was $1.007 \cdot 10^{-17}$. Consequently, we can confidently conclude that
485 *eif(iso)4e* plants are fully resistant to TuMV YC5 infection, regardless of the VPg allele
486 carried by the virus.
487 Many recessive resistance genes against potyviruses described in wild and crop
488 species encode members of the eIF(iso)4E and eIF(iso)4G families (Truninger and
489 Aranda 2009). Here, we have observed that TuMV YC5 replication strictly depends on
490 the interaction between VPg and a functional eIF(iso)4E. The complete resistance
491 observed for *eif(iso)4e* plants suggests its function cannot be complemented by other
492 translation initiation factors. By contrast, Navarro et al. (2022) were able of
493 experimentally evolving lineages derived from the YC5 isolate in *A. thaliana* mutants
494 *i4g1* (deficient for eIF(iso)4G1), observing different amino acid substitutions in VPg
495 associated with significant fitness increases. These results confirm that eIF(iso)4G is not
496 as essential as eIF(iso)4E for TuMV infection or that its function can be complemented
497 by other translation initiation factors.
498
499 **3.4. Disease progression in *rhd1* mutant plants depends on the VPg allele carried by**
500 **TuMV**
501 In stark contrast to *eif(iso)4e* plants, *rhd1* plants exhibited variable responses to infection
502 with the three TuMV variants. Firstly, concerning changes in infection rate (Fig. 3A),
503 the mean time to produce visible symptoms was the same for the three viral variants in
504 wild-type plants (log-rank test: $\chi^2 = 5.806$, 2 d.f., $P = 0.055$), averaging 6.817 ±0.151 dpi.
505 However, significant differences among VPg alleles were observed in *rhd1* plants ($\chi^2 =$
506 5.806, 2 d.f., $P = 0.002$): TuMV-VPg^{wt} produced visible symptoms at 7.000 ±0.218 dpi
507 (±1 SE), significantly later than TuMV-VPg^{D113G} (6.700 ±0.242; $\chi^2 = 3.881$, 1 d.f., $P =$
508 0.049) and TuMV-VPg^{R118H} (5.950 ±0.170; $\chi^2 = 16.028$, 1 d.f., $P < 0.001$), although the
509 difference between both mutants was not statistically significant ($\chi^2 = 3.839$, 1 d.f., $P =$
510 0.050). Therefore, we conclude that VPg^{D113G} and VPg^{R118H} accelerate the appearance of
511 disease symptoms in plants deficient for RHD1.
512 Secondly, Fig. 3B illustrates the disease progression curves for the three virus
513 variants in both wild-type and *rhd1* plants. In wild-type plants, large and significant inter-
514 individual differences were observed between the three VPg alleles ($F_{2,57} = 45.487$, $P <$

515 0.001, η_P^2 = 0.615), as well as substantial intra-individual differences between dpi
516 ($F_{3.933,224.203}$ = 502.504, P < 0.001, η_P^2 = 0.898) and the interaction between intra- and
517 inter-individual factors ($F_{7.867,224.203}$ = 13.586, P < 0.001, η_P^2 = 0.323). Overall, TuMV-
518 VPg^{wt} induced milder symptoms (0.879 ±0.043) compared to viruses expressing the two
519 mutant VPg variants (1.417 ±0.043 for VPg^{D113G} and 1.338 ±0.043 for VPg^{R118H}; pairwise
520 comparisons: P < 0.001). The progression of symptoms was similar for the three variants
521 during the first 7 dpi but diverged between VPg^{wt} and the two mutants thereafter. The
522 two mutant VPg variants were indistinguishable throughout the entire time course of the
523 experiment (P = 0.595). In the case of *rhd1* plants, inter-individual effects were large and
524 significant ($F_{2,57}$ = 8.322, P < 0.001, η_P^2 = 0.226), as were intra-individual effects of dpi
525 ($F_{2.790,159.046}$ = 293.746, P < 0.001, η_P^2 = 0.837), but not the interaction of the two factors
526 ($F_{5.581,159.046}$ = 2.090, P = 0.062, η_P^2 = 0.068). This suggests that differences among virus
527 variants remained constant over time. Overall, indistinguishable symptoms were induced
528 by TuMV-VPg^{wt} and TuMV-VPg^{D113G} (1.092 ±0.059 and 1.058 ±0.059, respectively; P
529 = 1.000), but both were significantly milder than those induced by TuMV-VPg^{R118H}
530 (1.371 ±0.059; $P \leq 0.005$).
531 Thirdly, we assessed the efficiency of TuMV carrying different VPg alleles in terms
532 of viral accumulation at 12 dpi. Fig. 3C illustrates the comparison between the two plant
533 genotypes and the three VPg alleles. The two orthogonal main factors had a significant
534 effect on viral load, although the magnitude of the effect was small among VPg alleles
535 (plant genotype: χ^2 = 226.733, 1 d.f., P < 0.001, η_P^2 = 0.459; VPg allele: χ^2 = 75.113, 2
536 d.f., P < 0.001, η_P^2 = 0.065). Nonetheless, the interaction between both factors was highly
537 significant and of large magnitude (χ^2 = 196.689, 2 d.f., P < 0.001, η_P^2 = 0.353), suggesting
538 that the effect on viral load of the VPg alleles was strongly dependent on the expression
539 of *RHD1*. As illustrated in Fig. 3C, viral load was reduced, on average, by 47.93% in
540 *rhd1* plants ($P \leq 0.018$ in the three pairwise comparisons). Focusing on wild-type plants,
541 TuMV-VPg^{R118H} showed the highest log-viral load (7.839 ±6.200; ±1 SE), followed by
542 TuMV-VPg^{wt} (7.754 ±6.122) and TuMV-VPg^{D113G} (7.563 ±5.992). However, in *rhd1*
543 plants, the situation reversed, and the highest log-viral load was observed for TuMV-
544 VPg^{D113G} (7.597 ±6.515), followed by TuMV-VPg^{wt} (7.329 ±5.824) and TuMV-VPg^{R118H}
545 (7.375 ±5.997), showing very similar accumulations ($P \leq 0.031$ in the three pairwise
546 comparisons).

547 At first glance, the observation of earlier and more severe symptoms in *rhd1* plants
548 suggests that the RHD1 protein plays an antiviral role in *A. thaliana*. However, higher
549 TuMV accumulation was noted in wild-type plants. To reconcile these two observations,
550 one could argue that symptoms may not necessarily correlate with viral accumulation if
551 *RHD1* enhances the plant's tolerance to viral infection (Pagán and García-Arenal 2020).
552 In such a scenario, wild-type plants expressing *RHD1* might exhibit higher viral
553 accumulation while maintaining mild symptoms. Conversely, if *RHD1* expression is
554 knocked out, even low viral accumulation could rapidly result in more severe symptoms.
555 Interestingly, the level of tolerance appears to be influenced by VPg alleles: viruses
556 carrying the wild-type and R118H alleles demonstrate larger reductions in virus
557 accumulation, whereas viruses carrying the generalist D113G allele are less affected (Fig.
558 3C).
559 Together with RMB1 and ROS1-ASSOCIATED WD40 DOMAIN-
560 CONTAINING PROTEIN (RWD40), RHD1 is part of the RWD40 complex, which
561 regulates active DNA demethylation by specifically directing ROS1 DNA demethylase
562 to specific target sequences in the *A. thaliana* genome (Liu et al. 2021). The absence of
563 expression of any of the components of the RWD40 complex results in ROS1
564 mislocalization, hypermethylation of targeted genomic DNA regions and
565 hypersusceptibility to the hemibiotrophic bacterial pathogen *Pseudomonas syringae*,
566 suggesting a role of the RWD40 DNA demethylation complex in pathogen defense (Liu
567 et al. 2021). One of these regions is localized in the *ROS1* promoter, leading to slightly
568 increased *ROS1* expression. Therefore, in *rhd1* plants, *ROS1* expression is upregulated
569 but its methylated target sequences are not recognized and become hypermethylated in
570 compared to wild-type plants. In addition, TuMV infection also downregulates the
571 expression of *ROS1* (Corrêa et al. 2020), in agreement with the results shown for wild-
572 type plants in Fig. 2 for most dpi. The sharp *RHD1* induction observed during TuMV
573 infection might be involved in temporally downregulating *ROS1* expression and the
574 subsequent temporal increase in the methylation rate of specific genome sequences,
575 thereby altering gene expression. Moreover, the pulse-like expression of *RHD1* and the
576 drop in expression in *TGA1* observed after 6 dpi (Fig. 2) coincides with the slow-down
577 in symptoms progression observed for TuMV-VPg^{wt}, which stay subsequently milder
578 (roughly speaking in the range 1 to 2). The two VPg mutants escape from this control,
579 resulting in worsened symptoms.
580

581 **3.5. Integrating interaction results with structural analyses**

582 To better understand these differences in interactions, we modeled the interactions of VPg
583 with eIF(iso)4E (Fig. 4) and RHD1 (Fig. 5). First, we modeled the TuMV-
584 VPg/eIF(iso)4E complex using a docking procedure guided by experimental data
585 (Supplementary Fig. S2). Several lines of evidence suggest that the proposed model is
586 close to the real structure: (*i*) the contact surface involves the central domain of VPg and
587 the cap-binding region of eIF(iso)4E, in agreement with experimental data; (*ii*) conserved
588 residue R103 in the central domain of VPg binds to eIF(iso)4E in a position equivalent to
589 the guanine base in the m^7G cap, (*iii*) acidic residues in the segment comprising the α1-
590 α2 loop bind to a region close to the phosphate binding region in eIF(iso)4E, (*iv*)
591 experimental data on residues involved int eIF4E - VPg interactions are mostly clustered
592 in the docking interaction surface (Grzela et al. 2006; Roudent-Tavert et al. 2007; Ashby
593 et al. 2012; Svanella-Dumas et al. 2014; Coutinho de Oliveira et al. 2019). Our model
594 also provides a plausible explanation of the effect of the R118H and D113G substitutions
595 on the eIF(iso)4E - VPg interaction (Fig 4). R118 and D113 are located in a small helical
596 segment predicted to bind to a variable region of complementary charge in eIF(iso)4E in
597 the m^7G cap binding pocket (Fig. 4). Both mutants are predicted to have a significant
598 effect on the net charge with respect to the VPg^{wt} (pI ≈ 7.23), with D113G making the
599 protein more positive (pI ≈ 8.02) and R118H more negative (pI ≈ 6.74). Therefore, we
600 postulate that these pI changes in the R118H and D113G mutants remove favorable ionic
601 interactions, resulting in the observed reduction in the stability of the eIF(iso)4E - VPg
602 complex.

603 Our model also explains the resistance of *eif(iso)4e* plants against the three TuMV
604 mutants. Potyviruses selectively require different eIF4E paralogs to establish infection
605 (Duprat et al. 2002; Sato et al. 2005; Nicaise et al. 2007; Gómez et al. 2019). In *A.*
606 *thaliana*, lettuce mosaic virus (LMV), TEV and TuMV use eIF(iso)4E, while other
607 potyviruses, such as clover yellow vein virus and PVY, use eIF4E (Sato et al. 2005;
608 Zafirov et al. 2023). Structurally, one of the most salient differences between eIF(iso)4E
609 and its paralogs eIF4E and nCBP is the presence of a bulkier segment in the VPg binding
610 region. We propose that due to this steric effect, neither eIF4E nor nCBP can substitute
611 for eIF(iso)4E in the *eif(iso)4e* plants (Fig. 4).

612 We also used docking to identify a potential VPg binding pocket in the RHD1
613 protein from *A. thaliana* (Fig. 5). A prediction of structural domains revealed that this

614 protein contains an N-proximal Zn finger domain, a C-terminal homeobox domain and
615 two unstructured segments comprising the N-terminal and central regions (Fig. 5A).
616 Assuming that binding occurs in the homeobox regions, we performed a global docking
617 of VPg against the homeobox domains using a refined AlphaFold model of RHD1 (Fig.
618 5B). The lowest energy complex fitted the VPg core domain within a crevice separating
619 the helical and beta-stranded regions of the ZF-HD homeobox. This region comprises
620 domains of positive and negative charge that might be affected by the ionization state of
621 the VPg protein.
622 Fig. 5C shows the RHD1 PPIs network generated with STRING. Interestingly,
623 RHD1 interactors mostly belong to the ZF-HD-containing family protein of transcription
624 factors. The direct interactor PATHOGENESIS RELATED HOMEODOMAIN
625 PROTEIN A (PRHA) is a hub that bridges ZF-HDs involved in the regulation of different
626 aspects of plant development and of circadian clock, with MVA3.30, a disease resistance
627 protein of the TIR-NBS-LRR class family, and with MORPH RELATED GENE 1
628 (MRG1) and 2 (MRG2), both readers of H3K4m3/H3K36m3 methylation marks. Taken
629 together, these interactions suggest that VPg affects epigenetic regulations by directly
630 interacting with RHD1 and indirectly affecting its interaction with other transcription
631 factors and with components of the histone methylation machinery. The role of such
632 epigenetic pathways in TuMV infection has been already stablished (Corrêa et al. 2020;
633 Navarro et al. 2022) and might contribute to the enhanced tolerance to infection of plants
634 accumulating RHD1.
635
636

637 **4. Concluding remarks**

638 The results shown above shed light on the complex interplay between TuMV VPg
639 variants, host proteins, and plant defense response, providing valuable insights into the
640 molecular mechanisms underlying virus-host interactions and disease progression in *A.*
641 *thaliana*. The three different VPg alleles used in our study show differential interactions
642 with plant proteins. Infected plants show altered expression of key genes *eIF(iso)4E*,
643 *RHD1* and *TGA1*. Mutant plants *eif(iso)4e* show complete resistance to TuMV infection
644 regardless of the VPg allele, confirming its well described essential role in virus
645 replication. Finally, different VPg alleles affect disease progression in *rhd1* mutant
646 plants. VPg^{D113G} and VPg^{R118H} accelerate symptom appearance, while VPg^{wt} induces

milder symptoms. This observation suggests that RHD1 modulates the tolerance to viral infection, likely via epigenetic modifications.

Data availability

All raw data are available at https://git.csic.es/SFElena/tumv-evolution-in-a.-thaliana-genotypes-with-deficient-immune-responses.

Supplementary data

Supplementary data is available at *Virus Evolution* online.

Acknowledgments

We thank Francisca de la Iglesia and Paula Agudo for excellent technical assistance and the rest of the EvolSysVir lab members for fruitful discussions.

Funding

This work was supported by grants PID2022-136912NB-I00 funded by MCIU/AEI/10.13039/501100011033 and by "ERDF a way of making Europe", and CIPROM/2022/59 funded by Generalitat Valenciana. to S.F.E.

References

Agudelo-Romero, P. et al. (2008) 'Virus adaptation by manipulation of host's gene expression', *PLoS ONE*, 3: e2397.

Aguirre, J., and Guantes R. (2023) 'Virus-host protein co-expression networks reveal temporal organization and strategies of viral infection', *iScience*, 26: 108475.

Ahmed, H. et al. (2018) 'Network biology discovers pathogen contact points in host protein-protein interactomes', *Nature Communications*, 9: 2312.

678 Alamillo, J.M., Saénz, P., and García, J.A. (2006) 'Salicylic acid-mediated and RNA-
679 silencing defense mechanisms cooperate in the restriction of systemic spread of plum
680 pox virus in tobacco', *Plant Journal*, 48: 217-27.
681 Amari, K. et al. (2014) 'Myosins VIII and XI play distinct roles in reproduction and
682 transport of *Tobacco mosaic virus*', *PLoS Pathogens*, 10: e1004448.
683 Ambrós, S. et al. (2024) 'Phenotypic and genomic changes during turnip mosaic virus
684 adaptation to *Arabidopsis thaliana* mutants lacking epigenetic regulatory factors',
685 *Evolution*, 28: 69-85.
686 Ashby, J. A. et al. (2011) 'Structure-based mutational analysis of eIF4E in relation to
687 *sbm1* resistance to pea seed-borne mosaic virus in pea', *PLoS ONE*, 6: e15873.
688 Ayme, V. et al. (2006) 'Different mutations in the genome-linked protein VPg of potato
689 virus Y confer virulence on the *pvr2*^{3} resistance in pepper', *Molecular Plant-Microbe*
690 *Interactions*, 19: 557-63.
691 Belshaw, R., Pybus, O. G., and Rambaut, A. (2007) 'The evolution of genome
692 compression and genomic novelty in RNA viruses', *Genome Research*, 17: 1496-
693 504.
694 Bosque, G. et al. (2014) 'Topology analysis and visualization of *Potyvirus* protein-protein
695 interaction network', *BMC Systems Biology*, 8: 129.
696 Boyes, D. C. et al. (2001) 'Growth stage-based phenotypic analysis of Arabidopsis: a
697 model for high throughput functional genomics in plants', *Plant Cell*, 13: 1499-510.
698 Buschmann, H. et al. (2004) 'Helical growth of the *Arabidopsis* mutant *tortifolia1* reveals
699 a plant-specific microtubule-associated protein', *Current Biology*, 14: 1515-21.
700 Butković, A. et al. (2021) 'A genome-wide association study identifies *Arabidopsis*
701 *thaliana* genes that contribute to differences in the outcome of infection with two
702 turnip mosaic potyvirus strains that differ in their evolutionary history and degree of
703 host specialization', *Virus Evolution*, 7: veab063.
704 Cervera, H. et al. (2018) 'Viral fitness correlates with the magnitude and direction of the
705 perturbation induced in the host's transcriptome: the tobacco etch potyvirus-tobacco
706 case study', *Molecular Biology and Evolution*, 35: 1599-615.
707 Chastain, C. J. et al. (2007) 'The pyruvate, orthophosphate dikinase regulatory proteins
708 of Arabidopsis possess a novel, unprecedented Ser/Thr protein kinase primary
709 structure', *Plant Journal*, 53: 854-63.
710 Chaudhury, S. et al. (2011) 'Benchmarking and analysis of protein docking performance
711 in Rosetta v3.2'. *PLoS ONE*, 6: e22477.

712 Chen, C. C. et al. (2003) 'Identification of turnip mosaic virus isolates causing yellow
713 stripe and spot on calla lily', *Plant Disease*, 87: 901-5.
714 Conway, P. et al. (2014) 'Relaxation of backbone bond geometry improves protein energy
715 landscape modeling', *Protein Science*, 23: 47-55.
716 Corrêa, R. L. et al. (2020) 'Viral fitness determines the magnitude of transcriptomic and
717 epigenomic reprogramming of defense responses in plants', *Molecular Biology and*
718 *Evolution*, 37: 1866-81.
719 Coutinho de Oliveira, L. et al. (2019) 'Structural studies of the eIF4E-VPg complex reveal
720 a direct competition for capped RNA: implications for translation', *Proceedings of*
721 *the National Academy of Sciences of the USA*, 116: 24056-65.
722 Czechowski, T. et al. (2005) 'Genome-wide identification and testing of superior
723 reference genes for transcript normalization in Arabidopsis', *Plant Physiology*, 139:
724 5-17.
725 Czerkies, M. et al. (2018) 'Cell fate in antiviral response arises in the crosstalk of IRF,
726 NF-κB and JAK/STAT pathways', *Nature Communications*, 9: 493.
727 De Chassey, B. et al. (2008) 'Hepatitis C virus infection protein network', *Molecular*
728 *Systems Biology*, 4: 230.
729 Dominguez, C., Boelens, R., and Bonvin, A. M. (2003) 'HADDOCK: a protein-protein
730 docking approach based on biochemical or biophysical information', *Journal of the*
731 *American Chemical Society*, 125: 1731-7.
732 Du, P. et al. (2023) 'WRKY transcription factors and OBERON histone-binding proteins
733 form complexes to balance plant growth and stress tolerance', *EMBO Journal*, 42:
734 e113639.
735 Duprat, A. et al. (2002) 'The Arabidopsis eukaryotic initiation factor (iso)4e is
736 dispensable for plant growth but required for susceptibility to potyviruses', *Plant*
737 *Journal*, 32: 927-34.
738 Dyer, M. D., Murali, T. M., and Sobral, B. W. (2008) 'The landscape of human proteins
739 interacting with viruses and other pathogens', *PLoS Pathogens*, 4: e32.
740 Edgar, R. C. (2004) 'MUSCLE: multiple sequence alignment with high accuracy and
741 high throughput', *Nucleic Acids Research*, 32: 1792-7.
742 Eskelin, K. et al. (2011) 'Potyviral VPg enhances viral RNA translation and inhibits
743 reporter mRNA translation *in planta*', *Journal of Virology*, 85: 9210-21.
744 Gallois, J. L. et al. (2010) 'Single amino acid changes in the turnip mosaic virus viral
745 genome-linked protein (VPg) confer virulence towards *Arabidopsis thaliana* mutants

746 knocked out for eukaryotic initiation factors eIF(iso)4E and eIF(iso)4G', *Journal of*
747 *General Virology*, 91: 288-93.
748 German-Retana, S. et al. (2008) 'Mutational analysis of plant cap-binding protein eIF4E
749 reveals key amino acids involved in biochemical functions and potyvirus infection',
750 *Journal of Virology*, 82: 7601-12.
751 Gilkerson, J. et al. (2012) 'The plastid-localized pfkB-type carbohydrate kinases
752 FRUCTOKINASE-LIKE 1 and 2 are essential for growth and development of
753 *Arabidopsis thaliana*', *BMC Plant Biology*, 12: 102.
754 Gómez, M. A. et al. (2019) 'Simultaneous CRISPR/Cas9-mediated editing of cassava
755 eIR4E isoforms nCBP-1 and nCBP-2 reduce cassava brown streak disease symptom
756 severity and incidence', *Plant Biotechnology Journal*, 17: 421-34.
757 González, R., Butković, A., and Elena, S. F. (2019) 'Role of host genetic diversity for
758 susceptibility-to-infection in the evolution of virulence of a plant virus', *Virus*
759 *Evolution*, 5: vez024.
760 González, R. et al. (2021) 'Plant virus evolution under strong drought conditions results
761 in a transition from parasitism to mutualism', *Proceedings of the National Academy*
762 *of Sciences of the USA*, 118: e2020990118.
763 Grzela, R. et al. (2006) 'Potyvirus terminal protein VPg, effector of host eukaryotic
764 initiation factor eIF4E', *Biochimie*, 88: 887-96.
765 Hafrén, A., Löhmus, A., and Mäkinen, K. (2015) 'Formation of potato virus A-induced
766 RNA granules and viral translation are interrelated processes required for optimal
767 virus accumulation', *PLoS Pathogens*, 11: e1005314.
768 Hillung, J. et al. (2014) 'Experimental evolution of an emerging plant virus in host
769 genotypes that differ in their susceptibility to infection', *Evolution*, 68: 2467-80.
770 Honorato, R. V. et al. (2021) 'Structural biology in the clouds: the WeNMR-EOSC
771 ecosystem', *Frontiers in Molecular Biosciences*, 8: 729513.
772 Jumper, J. et al. (2021) 'Highly accurate protein structure prediction with AlphaFold',
773 *Nature*, 596: 583-9.
774 Liu, P. et al. (2021) 'A novel protein complex that regulates active DNA demethylation
775 in Arabidopsis', *Journal of Integrative Plant Physiology*, 63, 772-86.
776 Mahmoudabadi, G, and Phillips, R. (2018) 'A comprehensive and quantitative
777 exploration of thousands of viral genomes', *eLife*, 7: e31955.
778 Mandell, D. J. et al. (2009) 'Sub-angstrom accuracy in protein loop reconstruction by
779 robotics-inspired conformational sampling', *Nature Methods*, 6: 551-2.

780 Martínez, F. et al. (2016) 'Interaction network of tobacco etch potyvirus NIa protein with
781 the host proteome during infection', *BMC Genomics*, 17: 87.
782 Martínez, F. et al. (2023) 'A binary interaction map between turnip mosaic virus and
783 *Arabidoposis thaliana* proteomes', *Communications Biology*, 6: 28.
784 Melero, I., González, R. and Elena, S.F. (2023) 'Host developmental stages shape the
785 evolution of plant RNA virus', *Philosophical Transactions of the Royal Society B:*
786 *Biological Sciences*, 378: 20220005.
787 Menche, J. et al. (2015) 'Uncovering disease-disease relationships through the incomplete
788 interactome', *Science*, 347: 841.
789 Miras, M. et al. (2017) 'Structure of eIF4E in complex with an eIF4G peptide supports a
790 universal bipartite binding mode for protein translation', *Plant Physiology*, 174:
791 1476-91.
792 Monzingo, A. F. et al. (2007) 'The structure of eukaryotic translation initiation factor-4E
793 from wheat reveals a novel disulfide bond', *Plant Physiology*, 143: 1504-18.
794 Moury, B. et al. (2004) 'Mutations in potato virus Y genome-linked protein determine
795 virulence towards recessive resistances in *Capsicum annuum* and *Lycopersicon*
796 *hirsutum*', *Molecular Plant-Microbe Interactions*, 17: 322-9.
797 Mukhtar, M. S. et al. (2011) 'Independently evolved virulence effectors converge onto
798 hubs in a plant immune system network', *Science*, 333: 596-601.
799 Navarro, R. et al. (2022) 'Defects in plant immunity modulate the rates and patterns of
800 RNA virus evolution', *Virus Evolution*, 8: veac059.
801 Nicaise, V. et al. (2007) 'Coordinated and selective recruitment of eIF4E and eIF4G
802 factors for potyvirus infection in *Arabidopsis thaliana*', *FEBS Letters*, 581: 1041-6.
803 Pagán, I., and García-Arenal, F. (2020) 'Tolerance of plants to pathogens: an unifying
804 view', *Annual Review of Phytopathology*, **58**: 77-96.
805 Peremyslov, V. V. et al. (2008) 'Two class XI myosins function in organelle trafficking
806 and root hair development in Arabidopsis', *Plant Physiology*, 146: 1109-16.
807 Pérez, K. et al. (2012) 'Tobacco etch virus infectivity in *Capsicum* spp. is determined by
808 a maximum of three amino acids in the viral virulence determinant VPg', *Molecular*
809 *Plant Microbe Interactions*, 25: 1562-73.
810 Phillips, J. C. et al. (2020). 'Scalable molecular dynamics on CPU and GPU architectures
811 with NAMD', *Journal of Chemical Physics,* 153: 044130.
812 Pichlmair, A. et al. (2012) 'Viral immune modulators perturb the human molecular
813 network by common and unique strategies', *Nature*, 487: 486-90.

814 Roudet-Tavert, G. et al. (2007) 'Central domain of a potyvirus VPg is involved in the
815 interaction with the host translation initiation factor eIF4E and the viral protein
816 HCPro', *Journal of General Virology*, 88: 1029-33.
817 Rydzik, A. M. et al. (2017) 'mRNA cap analogues substituted in the tetraphosphate chain
818 with CX2: identification of O-to-CCl2 as the first bridging modification that confers
819 resistance to decapping without impairing translation'. *Nucleic Acids Research*, 45:
820 8661-75.
821 Sato, M. et al. (2005) 'Selective involvement of members of the eukaryotic initiation
822 factor 4E family in the infection of *Arabidopsis thaliana* by potyviruses', *FEBS*
823 *Letters*, 579: 1167-71.
824 Shearer, H.L. et al. (2012) 'Arabidopsis clade I TGA transcription factors regulate plant
825 defenses in an NPR1-independent fashion', *Molecular Plant Microbe Interactions*,
826 25: 1459-68.
827 Spivak, M. et al. (2023) 'VMD as a platform for interactive small molecule preparation
828 and visualization in quantum and classical simulations', *Journal of Chemical*
829 *Information and Modeling*, 63: 4664-78.
830 Sun, T. et al. (2018) 'TGACG-BINDING FACTOR 1 (TGA1) and TGA4 regulate
831 salicylic acid and pipecolic acid biosynthesis by modulating the expression of
832 *SYSTEMIC ACQUIRED RESISTANCE DEFICIENT 1* (*SARD1*) and
833 *CALMODULIN-BINDING PROTEIN 60g* (*CBP50g*)', *New Phytologist*, 217: 344-
834 54.
835 Svanella-Dumas, L. et al. (2014) 'Adaptation of lettuce mosaic virus to *Catharanthus*
836 *roseus* involves mutations in the central domain of the VPg', *Molecular Plant*
837 *Microbe Interactions*, 27: 491-7.
838 Szklarczyk, D. et al. (2023) 'The STRING database in 2023: protein-protein association
839 networks and functional enrichment analyses for any sequenced genome of interest',
840 *Nucleic Acids Research*, 50: gkac1000.
841 Tarazona, A., Forment, J., and Elena, S. F. (2020) 'Identifying early warning signals for
842 the sudden transition from mild to severe tobacco etch disease by dynamical network
843 biomarkers', *Viruses*, 12: 16.
844 Tisoncik-Go, J. et al. (2016) 'Integrated omics analysis of pathogenic host responses
845 during pandemic H1N1 influenza virus infection: the crucial role of lipid
846 metabolism', *Cell Host Microbe*, 19: 254-66.

847 Truninger, V., and Aranda M.A. (2009) 'Recessive resistance to plant viruses', *Advances*
848 *in Virus Research*, 75: 119-59.
849 Uetz, P. et al. (2006) 'Herpesviral protein networks and their interaction with the human
850 proteome', *Science*, 311: 239-42.
851 Van Zundert, G. C. P. et al. (2016) 'The HADDOCK2.2 web server: user-friendly
852 integrative modeling of biomolecular complexes', *Journal of Molecular Biology*,
853 428: 720-5.
854 Wan, X. et al. (2020) 'Discovery of lysine-targeted eIF4E inhibitors through covalent
855 docking'. *Journal of the American Chemical Society*, 142: 4960-4.
856 Wang, C., Bradley, P., and Baker, D. (2007). 'Protein-protein docking with backbone
857 flexibility', *Journal of Molecular Biology*, 373: 503-19.
858 Webb, B., and Sali, A. (2016) 'Comparative protein structure modeling using
859 MODELLER'. *Current Protocols in Bioinformatics*, 54: 5.6.1-37.
860 Wojcik, R. et al. (2021) 'Novel N7-arylmethyl substituted dinucleotide mrna 5' cap
861 analogs: synthesis and evaluation as modulators of translation', *Pharmaceutics*, 13:
862 1941.
863 Zafirov, D. et al. (2023) 'Arabidopsis *eIF4E1* protects the translational machinery during
864 TuMV infection and restricts virus accumulation', *PLoS Pathogens*, 19: e1011417.
865 Zavaliev, R., and Dong, X. (2023) 'NPR1, a key immune regulator of plant survival under
866 biotic and abiotic stresses', *Molecular Cell*, 84: 131-41.
867

868 **Figures**

869

870 **Figure 1.** Heatmap constructed from the estimated binding affinities between the three
871 different VPg alleles (wild-type, D113G and R118H) and the 19 host proteins identified
872 in the HT-Y2H screening. Gene names are only provided for interactors for which
873 statistically significant differences with VPg^{wt} were found and further identified by
874 sequencing. Interactors for which no significant differences in binding affinity were
875 observed are indicated in red. Labels starting with "dg" correspond to those found in the
876 screening against VPg^{D113G}, "rh" to those found in the screening against VPg^{R118H} and
877 "wt" against the VPg^{wt} allele. Color scale: the more intense blue corresponds to stronger
878 affinities than for VPg^{wt}, whereas stronger red corresponds to weaker affinities than for
879 VPg^{wt}.

880

881

882 **Figure 2.** Effect of TuMV VPg^{wt} infection upon expression of VPg direct (*RHD1*) and
883 indirect (*TGA1*) interactors. Significance levels (sequential Bonferroni *post hoc* tests: ***
884 $P < 0.001$.

885

886 **Figure 3.** (A) Survival curves representing the number of non-symptomatic plants along
887 time. (B) Progression of disease severity in wild-type and *rhd1* plants infected with
888 TuMV expressing the three different VPg alleles. Error bars represent 95% CI. (C)
889 Differences in viral load. Boxes represent interquartile ranks, horizontal lines the median
890 and error bars represent 95% CI. WT: wild-type plants.

891

892 **Figure 4.** Structural analysis of the *A. thaliana* eIF(iso)4E - TuMV VPg complex. (A)
893 The model of TuMV VPg reveals that D113 and R118 project outwards in a segment
894 comprising the α1-α2 loop and helix α2. The structural ensemble illustrates the
895 dynamical properties of the VPg proteins as determined by molecular dynamics
896 simulations. (B) Analysis of the eIF(iso)4E - VPg docking model suggests that residues
897 D113 and R118 bind to pockets of complementary charges in eIF(iso)4E. The reduced
898 affinity of the D113G and R118H variants probably results from the removal of these
899 ionic interactions. (C) The eIF(iso)4E - VPg (left) docking model explains the resistance
900 in *eif(iso)4e* plants as the paralogous protein eIF4E and nCBP have a bulkier VPg binding
901 region (L3) that is likely to impede binding to TuMV VPg (center). The sequence of the

902 L3 region of the eIF4E homologs in *A. thaliana* and their relative distance to VPg is
903 illustrated in the right panel.
904
905 **Figure 5.** Structural properties of the RHD1 protein from *A. thaliana*. (A) The
906 AlphaFold modeling and sequences analysis reveal that this protein contains Zn-finger
907 (ZF-HD) and a C-terminal homeobox domain, and unstructured N-terminal and central
908 regions. (B) Global docking of VPg against the homeobox domains of RHD1using
909 ROSETTA revealed a potential binding site comprising the central domain of VPg and a
910 crevice in the ZF-HD homeobox region. (C) PPI network of the RHD1 with other *A.*
911 *thaliana* proteins according to STRING database.

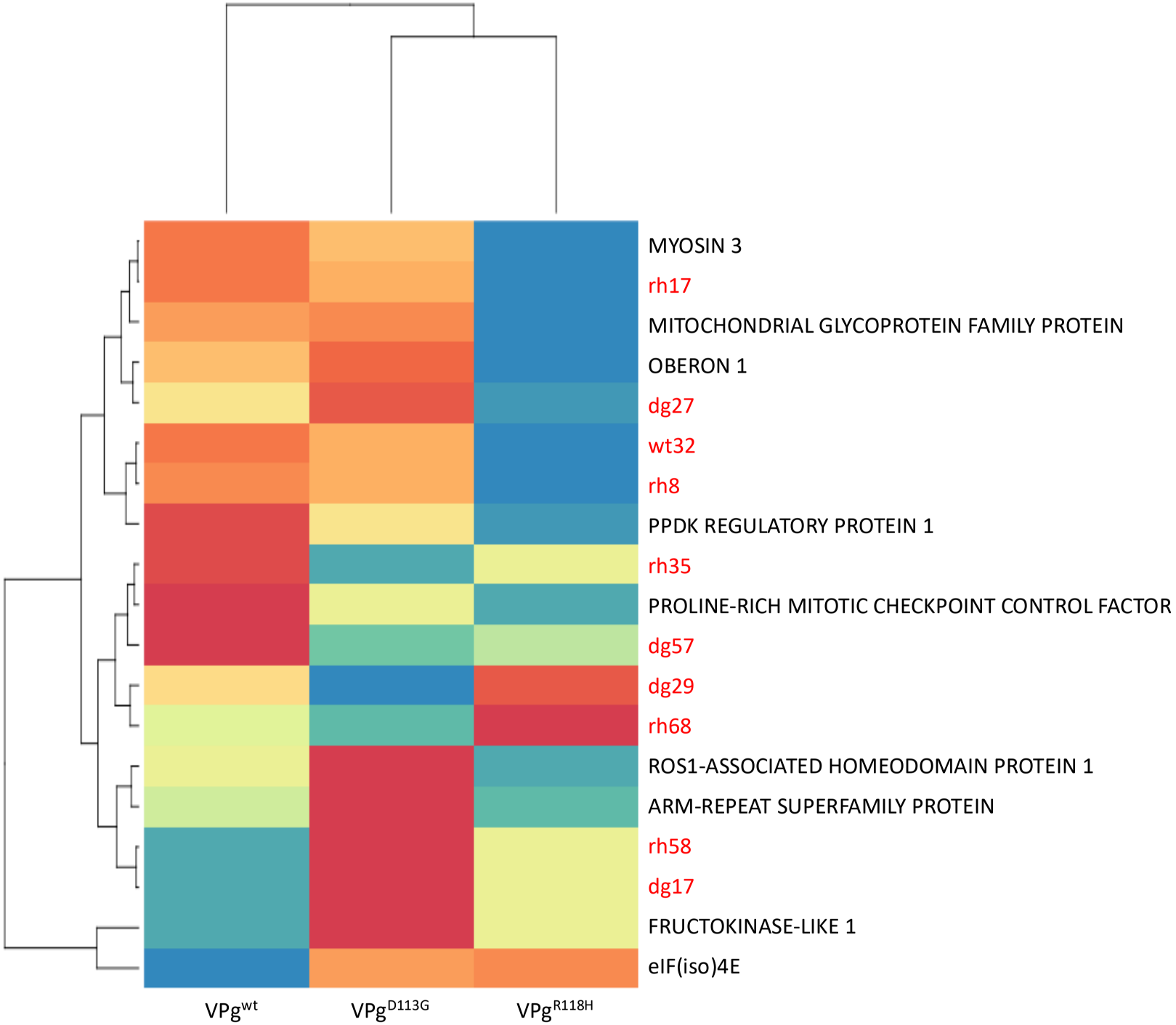
MYOSIN 3
rh17
MITOCHONDRIAL GLYCOPROTEIN FAMILY PROTEIN
OBERON 1
dg27
wt32
rh8
PPDK REGULATORY PROTEIN 1
rh35
PROLINE-RICH MITOTIC CHECKPOINT CONTROL FACTOR
dg57
dg29
rh68
ROS1-ASSOCIATED HOMEODOMAIN PROTEIN 1
ARM-REPEAT SUPERFAMILY PROTEIN
rh58
dg17
FRUCTOKINASE-LIKE 1
eIF(iso)4E
VPg^wt
VPg^D113G
VPg^R118H

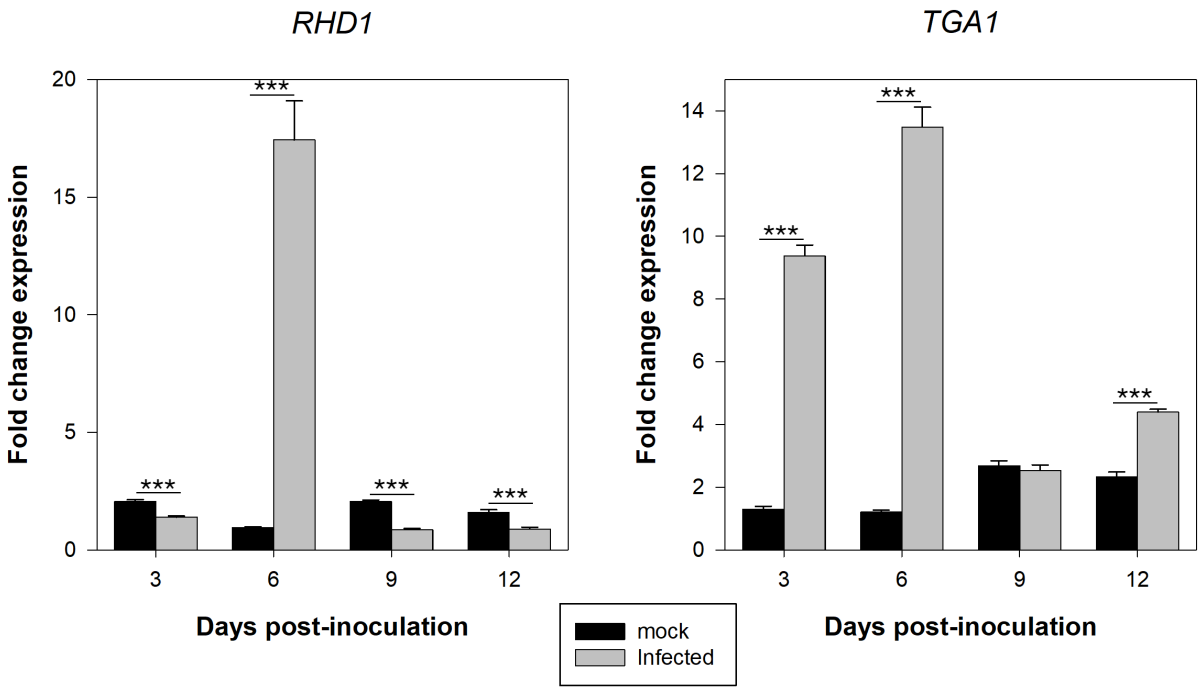
RHD1
TGA1
Fold change expression
Days post-inoculation
***
mock
Infected
0
5
10
15
20
2
4
6
8
12
14
3
6
9
12

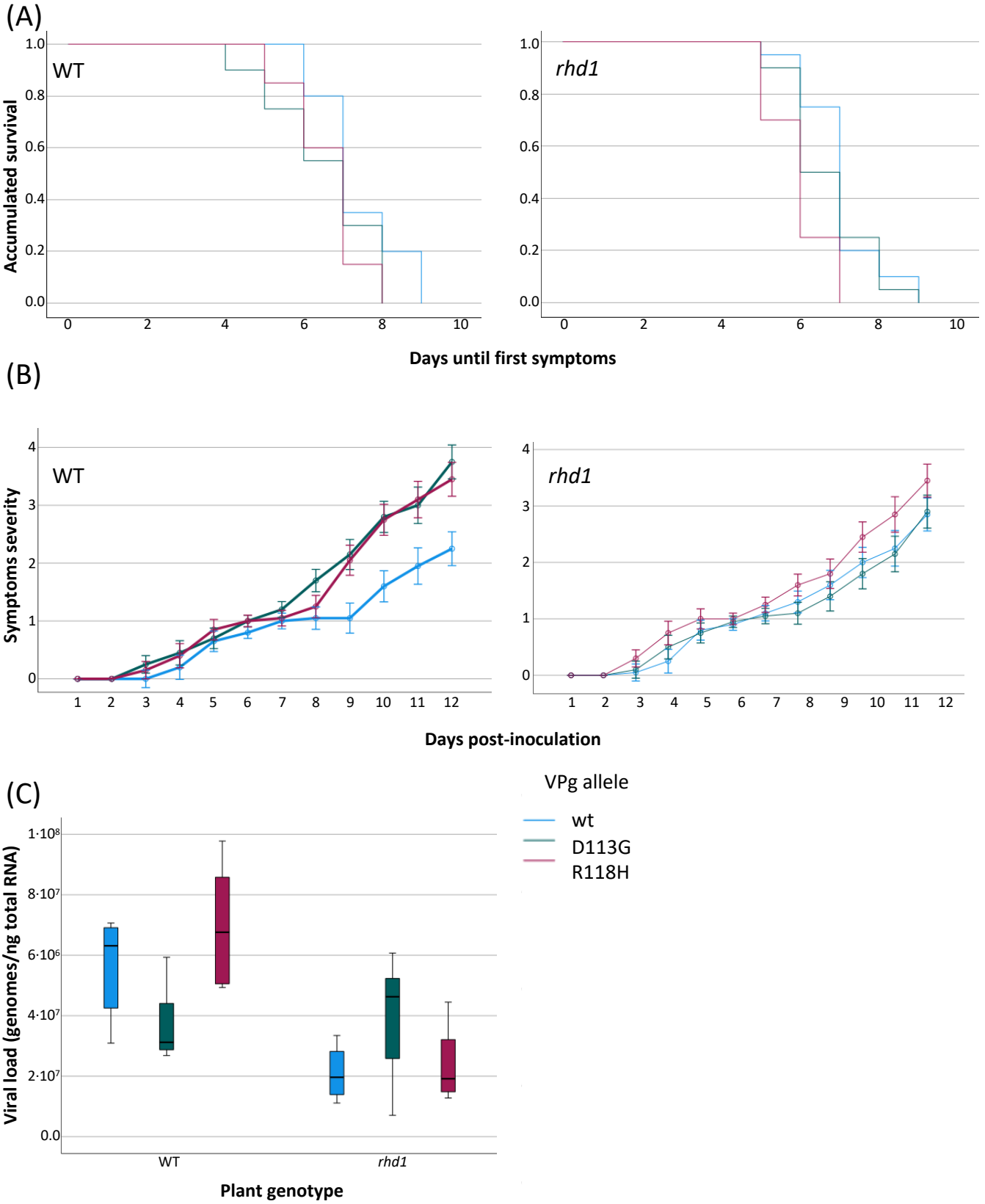
(A)
WT
rhd1
Accumulated survival
1.0
0.8
0.6
0.4
0.2
0.0
0
2
4
6
8
10
Days until first symptoms
(B)
WT
rhd1
Symptoms severity
4
3
2
1
0
1
2
3
4
5
6
7
8
9
10
11
12
Days post-inoculation
(C)
Viral load (genomes/ng total RNA)
1·10⁸
8·10⁷
6·10⁶
4·10⁷
2·10⁷
0.0
WT
rhd1
Plant genotype
VPg allele
wt
D113G
R118H

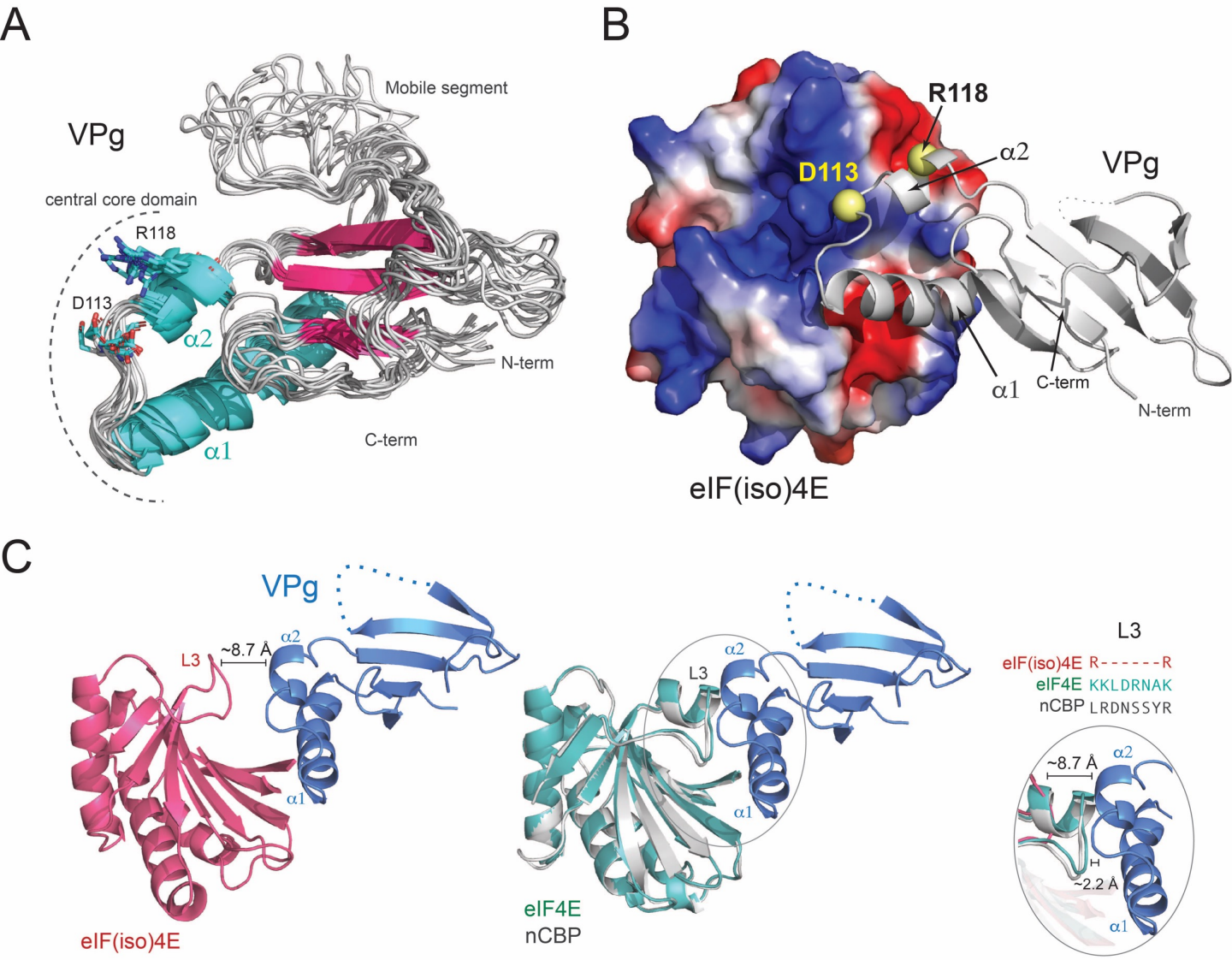
A
VPg
Mobile segment
central core domain
R118
D113
α2
α1
N-term
C-term
B
R118
D113
α2
VPg
α1
C-term
N-term
eIF(iso)4E
C
VPg
L3
~8.7 Å
α2
α1
eIF(iso)4E
L3
α2
α1
eIF4E
nCBP
L3
eIF(iso)4E R------R
eIF4E KKLDRNAK
nCBP LRDNSSYR
~8.7 Å
α2
H
~2.2 Å
α1

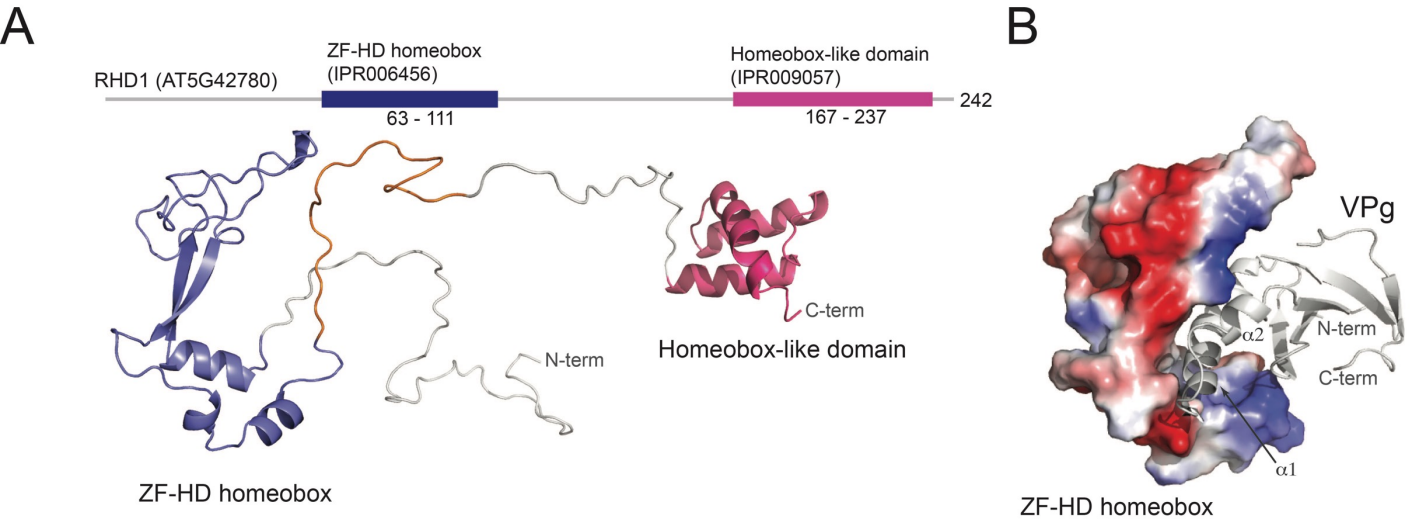

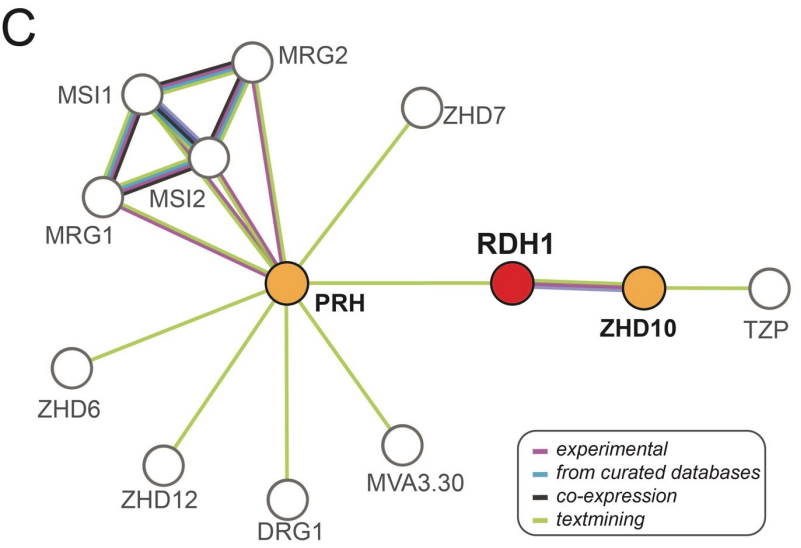

DRG1: Developmentally-regulated G-protein 1(AT1G17470)
MRG1: Protein MRG1 (AT4G37280)
MRG2: Protein MRG2 (AT1G02740)
MSI1: Histone-binding protein MSI1 (AT5G58230)
MSI2: WD-40 repeat-containing protein MSI2 (AT2G16780)
MVA3.30: Disease resistance protein (AT5G17680)
PRH: Pathogenesis-related homeodomain protein (AT4G29940)
TZP: Zinc knuckle (CCHC-type) family protein (AT5G43630)
ZHD10: Zinc-finger homeodomain protein 10 (AT5G39760)
ZHD12: Zinc-finger homeodomain protein 12 (AT5G604809
RDH1: Zinc-finger homeodomain protein 13 (AT5G42780)
ZHD6: Zinc-finger homeodomain protein 6 (AT2G18350)
ZHD7: Zinc-finger homeodomain protein 7 (AT3G50890)